DOI: 10.1002/fuce.201800164

Direct One-pot Synthesis of Carbon Supported Ag-Pt Alloy Nanoparticles as High Performance Electrocatalyst for Fuel Cell Application

T. Fu[1], S. Zhang[2], J. Huang[2], D. Cai[2], J. Li[2], J. Zhao[2]*

[1] Longyan University, Collaborative Innovation Center of Clean Energy, Longyan, 364012, Fujian, China
[2] Xiamen University, State Key Lab of Physical Chemistry of Solid Surfaces, College of Chemistry and Chemical Engineering, Collaborative Innovation Center of Chemistry for Energy Materials, State-Province Joint Engineering Laboratory of Power Source Technology for New Energy Vehicle, Xiamen, 361005, Fujian, China

Received November 04, 2018; accepted February 18, 2019; published online March 28, 2019

Abstract

Ag-Pt alloy material is one of the most potential candidates to improve the catalytic activity of Pt-based catalyst toward the oxygen reduction reaction (ORR), which can reduce the dosage of the high-cost metal Pt used in the cathode of fuel cells. But it is hard to synthesis Ag-Pt alloy with nanosize in an easy and cheap way. In this study, the Ag-Pt alloy nanoparticles supported on carbon (Ag-Pt/C) with different Ag at.% were prepared by a facile one-pot approach with low costs. The XRD, TEM and XPS measurements were applied to verify the alloy structure of Ag-Pt nanoparticles. These Ag-Pt/C samples showed enhanced mass activities and catalytic stabilities for the ORR, which was up to two times higher than that of the commercial Pt/C catalyst at 0.9 V (*vs.* reversible hydrogen electrode). Furthermore, the membrane electrode assembly (MEA) made from the Ag-Pt/C catalyst also showed a higher power density in H_2-O_2 fuel cell test compared to the MEA made from the commercial Pt catalyst. These enhancements are attributed to the higher utilization of Pt and the regulated oxygen adsorption energy of Pt in the surface, which was confirmed using the density function theory calculation.

Keywords: Ag-Pt Alloy, Electrocatalysis, Electrocatalyst, Fuel Cell, Membrane Electrode Assembly (MEA), Oxygen Reduction Reaction (ORR), Proton Exchange Membrane Fuel Cells (PEMFC), Supported Catalysts

1 Introduction

Fuel cells have great potential in the field of new energy applications, because of its high energy conversion efficiency, extreme energy density, zero-pollution and other advantages [1–4]. However, there is still a long way for the practical application of fuel cells on a large-scale since some technical problems remain to be solved. The low catalytic performance of catalyst for fuel cell cathode is one of the key problems. The reaction at the fuel cell cathode is the oxygen reduction reaction (ORR), and the optimal catalyst for the ORR is made by pure platinum (Pt) metal and carbon black, which is still not powerful enough for catalyzing ORR. Therefore, in order to ensure the output power of the fuel cells, a large dosage of the Pt metal is needed to be used in the cathode of fuel cells, while Pt is expensive and rare in the earth. As a result, the costs of fuel cell are too high, which is not conducive for the commercial promotion of fuel cells [5, 6].

The idea of solving this problem is reducing the dosage amount of the Pt metal while maintaining its catalytic performance for ORR [7, 8]. If an excellent Pt-based catalyst with a higher ORR catalytic performance and lower costs can be realized, the quality of the Pt metal used in a fuel cell will be reduced, meanwhile the cell costs will be significantly reduced. Tian and coworkers have improved the intrinsic catalytic activity of the surface of Pt metal by preparing the Pt nanoparticles with high-index crystal plane [9]. Also, reducing the amount of Pt in the catalyst by doping the non-noble met-

[*] *Corresponding author, jbzhao@xmu.edu.cn*

als into the Pt is another way to reduce the costs and enhance the catalytic performance of Pt-based catalyst [10–12]. For example, Schalow and Zhang have reduced the platinum content of the catalyst by using the multiple structures of Pt and other metal like core-shell structure [13, 14]. Meanwhile, the platinum-free metal catalysts [15, 16] and non-metallic catalysts [17–19] for the ORR have become a hotspot of the ORR research too. Furthermore, the highly efficient yttria-stabilized zirconia materials prepared by electrophoretic deposition possess controllable morphology [20, 21] and the novel materials with interfacial lattice-strain effects have a suitable electronic structure[22, 23], which also show a great potential in ORR catalysis and fuel cell cathode application.

In the above mentioned methods, alloying the Pt with other metal is an effective method to prepare a novel ORR catalyst with lower cost and improved ORR performance. Stamenkovic and coworkers have reported that the (111) surface of Pt_3Ni alloy has a very high intrinsic activity for the ORR, which is theoretically up to 80 times as high as the (111) surface of Pt [24]. Thus, the Pt-based alloy catalysts have caught the attention of many researchers. Throughout the summary of a large number of studies, it has been found that the performance of Pt-based alloys is improved because the other metal atoms are introduced to tune the Pt electronic structure. As the d-band center of the Pt surface of the catalyst decreases to a suitable location, its catalytic performance is effectively enhanced [25–27].

Silver (Ag) is a cheap metal with a price far lower than Pt, although its electronic structure is similar to that of Au and Cu, according to the Nørskov's theoretical calculation work, the catalytic activity of Ag for ORR may also at a high rate [28]. Besides, the lattice parameters of Ag metal are similar to that of Pt metal, indicating that they are easy to grow together to form an alloy [29]. Hence, Ag has a potential to form an alloy catalyst with Pt to exhibit excellent ORR catalytic properties. Up to now, there are many works on the Pt based alloys, and researchers have tried many combinations of Pt and various metals. We have reported the hollow Ag-Pt bimetallic catalyst (with average sizes of 17 nm [30] and 7 nm [31]) with excellent ORR performance. There are a few studies about the Ag-Pt dendrite (~250 nm) [32], hollow Ag-Pt chain (~50 nm) [33] and hollow Ag-Pt alloy (~100 nm) [34], which also shows the potential of the Ag-Pt alloy in the ORR catalyzing. However, there is few study on the high quality carbon supported Ag-Pt alloy with smaller size (< 5 nm) used as an ORR catalyst [35], which may be due to the high difficulty in directly synthesizing Ag-Pt alloy using a simple one-pot method, because the frequently-used cheap Pt salts usually contain Cl ions which would form AgCl precipitate instead during the co-reduction process.

In this work, a simple one-pot synthesis has been designed to prepare the Ag-Pt alloy nanoparticles loaded on carbon (Ag-Pt/C) with an average diameter of 4 nm, and the mechanism of the catalytic properties of Ag metal in Ag-Pt alloy has also been studied. This method has following advantages: (i) K_2PtCl_4, which is easy to get, is used as the Pt sources to prepare Ag-Pt alloy, but there is no AgCl precipitate formed during the preparation process; (ii) compared to other high temperature synthesis methods, its reaction temperature is only 120 °C, which does not consume too much energy in the synthesis, and has a high energy efficiency; (iii) not any surfactant is used in order to avoid the problem that the coverage of the surfactant on the catalyst surface will block the contact of the catalyst with oxygen, resulting in a low catalytic performance of oxygen reduction; (iv) the bimetallic nanoparticles are directly loaded on the carbon supports to avoid the agglomeration of nanoparticles. Compared with the commercial Pt/C catalyst, the as-prepared Ag-Pt/C catalyst shows a preferable ORR performance and the catalytic stability in the electrochemical rotating disk electrode (RDE) testing and the H_2–O_2 fuel cell test.

2 Experimental

2.1 General Materials

The silver nitrate (99.8%) and sodium borohydride (98%) were bought from Aladdin Company. The anhydrous ethanol (AR), perchloric acid (AR), ammonia solution (30 wt.%), isopropanol (AR) were received from Shanghai Sinopharm. And the ethylene glycol (EG, AR) was purchased from Xilong Science Co. Ltd. The Vulcan XC-72R carbon support came from Cobalt. Nafion ionomer (5 wt.%) was bought from Dupont and the commercial Pt/C was obtained from Johnson Matthey (HiSPEC™ 4000 for Pt 40 wt.% and HiSPEC™ 9100 for Pt 60 wt.%). The carbon monoxide (99.9%), nitrogen (99.999%) and oxygen (99.999%) were purchased from Xinhang Air Co. Ltd. (Xiamen, China).

The materials were directly used after receiving, and the purity of other reagents was analytical grade.

2.2 Synthesis of Ag-Pt Alloy Nanoparticles Loaded on Carbon (Ag-Pt/C)

The Ag-Pt/C catalysts were obtained by a one-pot synthesis. First, $AgNO_3$ of 8.0 mg or other amount, 19.5 mg K_2PtCl_4 (the Pt content of the Ag-Pt/C was fixed to be about 40 wt.% in the final product for comparing with the commercial Pt/C catalyst of 40 wt.% Pt), 1.0 mL ammonia solution and 0.5 mL DMF were mixed by ultrasonic treatment. After standing for 6 h, the color of the solution turned green, and then the mixed solution was added into a mixture of 30.0 mL ethylene glycol and 14.0 mg commercial carbon support. Then keeping this hybrid solution at 120 °C for 6 h, so that the Ag-Pt alloy catalyst loaded on the carbon support (Ag-Pt/C) can be formed successfully. After the reaction finished, the products were separated by centrifugation, then washed by water/ethanol for three times, and dried for 6 h at 60 °C in vacuum. Finally, the products were grinded into fine powder for further characterization. The experimental process is as displayed in Figure 1.

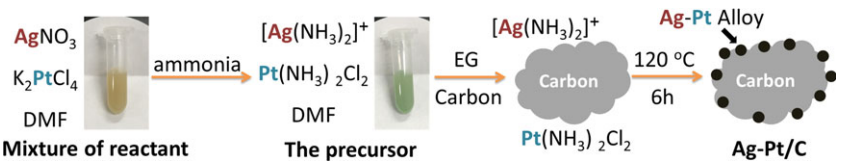

Fig. 1 The experimental process of the synthesis of Ag-Pt/C.

2.3 Characterization of Structure and Morphology

The crystal information of the catalysts was analyzed by X-ray diffraction (XRD) method. XRD patterns were obtained from the Mini Flex 600X-ray diffractometer (Rigaku) using Cu Kα radiation. The voltage was 40 kV and the current was 30 mA. The sample was dispersed in the ethanol, and then dripped on a glass slide to form a sample layer for testing. The test was carried out in a step scan mode at the scan speed of 2.0 ° min^{-1}.

The morphology of the samples were observed by TEM method, using the Holland FEI Tecnai F-30 HRTEM (300 kV), the crystal structure and the elemental distribution of the sample were also characterized by the F-30 at the same time with the help of the energy dispersive X-ray spectroscopy (EDS) and the selected area electron diffraction (SAED). The sizes and lattice fringes of the nanoparticles were analyzed by the Gatan Digital Micrograph software. The sample was dispersed in the ethanol and dropped on a copper grid for TEM characterization.

We also used ICP-AES method to determine element contents of the samples, the tests were performed by inductively coupled plasma (ICP, NCS Testing Technology, Plasma 1000). The samples were dissolved completely with aqua regia of a fixed volume, and the liquid supernatant was tested after the sedimentation of the carbon support.

The X-ray photoelectron spectroscopy (XPS) tests for characterizing the valence state of the elements were carried out by a Quantum-2000 X-ray scanning probe electron spectroscopy (PHI, United State) with Al Kα radiation, and 284.6 eV is the value of C_{1s} spectrum for adjusting the binding energy.

2.4 Electrochemical Measurements

The electrochemical performances of the samples were measured on a CHI 730E workstation with a three-electrode cell. The KCl-saturated Ag/AgCl electrode was chosen to be the reference electrode and then convert to reversible hydrogen electrode (RHE) by calculation, and a graphite electrode was used as the counter electrode. First, the dry sample of required amount was mixed with 980 μL ethanol and 20 μL Nafion ionomer (5 wt.%), and then mixed by ultrasonic for 3 h. After that, 10 μL mixture was loaded dropwise onto a rotating disk electrode (a surface area of 0.247 cm^2, PINE), and dried naturally. The loading amount of Pt on the electrode surface should be restrained in 3 μg.

We used a CO-stripping measurement to analyze the electrochemical surface area (ECSA) of the samples. The scan rate of the test was 50 mV s^{-1}, and the electrolyte was 0.1M $HClO_4$. The ECSA is calculated based on the ratio of the total charge of the subtracted CO adsorption peak to the 420 mC cm^{-2} (the specific charge of the CO monolayer adsorption). The ORR catalytic activity of samples was measured by linear scanning voltammetry (LSV). The electrolyte of the test was 0.1M $HClO_4$ with oxygen saturation. The scanning speed was 10 mV s^{-1}, and the rotating speed of the rotating disk electrode was 1,600 rpm. The accelerated durability test (ADT) was implemented in 0.1M $HClO_4$ with oxygen saturation by potential scanning between 0.6 and 1.0 V for 15,000 cycles at a scanning speed of 50 mV s^{-1}. The electrochemical tests above were all carried out at 25 °C.

The Ag-Pt/C sample with Ag content of 15 at.% (Ag-Pt/C-15%$_{Ag}$) was made into the membrane electrode assembly (MEA) by a traditional gas diffusion layer (GDL) method. The carbon paper (as the GDL) of the cathode with a Pt loading of 0.597 mg cm^{-2} was painted with the Ag-Pt/C ink made of mixing the Ag-Pt/C sample, Nafion ionomer and isopropanol, and the carbon paper of anode with a Pt loading of 0.358 mg cm^{-2} was painted with the Pt/C ink made by mixing the commercial Pt/C catalyst (JM, 60%), Nafion ionomer and isopropanol. The two carbon papers were hot-pressing with the Nafion under 80 °C under 5 MPa for 5 min to form the MEA. The whole Pt loading of the MEA using the Ag-Pt/C catalyst was 0.955 mg cm^{-2}, and the total metal loading was 1.013 mg cm^{-2}.

The standard MEA made with the commercial Pt/C catalyst (JM, 60 wt.% Pt) was established by the same method, but the catalyst used in the cathode side was also the commercial Pt/C catalyst (JM, 60% Pt). The Pt loading of the cathode side and the anode side was 0.650 mg cm^{-2} and 0.365 mg cm^{-2}, respectively, and the total Pt loading of the standard MEA was 1.015 mg cm^{-2}.

The H_2–O_2 fuel cell tests were carried out on the Arbin tester using a test fixture with 4 cm^2 flow field area. The flowing rate of oxygen and hydrogen gas was 0.15 slpm (standard liter per minute) with a 60% relative humidity. The fuel cell was operated under 70 °C. And before being tested, the MEA was run at a fixed current density of 0.050 A cm^{-2} for 24 h to be fully activated.

2.5 Density Function Theory (DFT) Calculation

The slabs (Figure S5) were built from (2 × 2) unit cells for the oxygen coverage of 0.25. And 12 Å was set to be the vacuum layer of the calculated slabs we used.

The oxygen adsorption energy was calculated using the Eq. (1):

$$\Delta E_O = E(slab + O) - E(slab) - 1/2E(O_2) \quad (1)$$

The oxygen adsorption energy of the surface of the slabs was calculated by Vienna *ab initio* simulation package (VASP)

ORIGINAL RESEARCH PAPER

[36] and the projector augmented-wave (PAW) approach [37]. The exchange-correlation functional is described by Perdew, Bruke, and Ernzerhof (PBE) [38] with the generalized gradient approximation (GGA) as the parameter. According to our convergence test, the 550 eV was configured to be the energy cutoffs for all the calculations. And the valence states of O (2s2p), Pt (6s5d), and Ag (5s4d) are for solving the Kohn-Sham equations.

3 Results and Discussion

3.1 Structure and Morphology of the Samples

Figure 2a shows the XRD pattern of the sample, which was synthesized by directly heating two kinds of metal salts with the carbon support in ethylene glycol. The comparison among the sample patterns and the standard Pt pattern (JCPDS number: 04-0802), Ag pattern (JCPDS number: 04-0783), AgCl pattern (JCPDS number: 31-1238) indicates that, without the preparation of precursor solution, the main components of this sample are pure Pt metal and AgCl, which are not consistent with our expected Ag-Pt alloys. The reason for this case is that the Pt salt used in our experiments is K_2PtCl_4, which contains Cl ions, and the Ag ions will combine with Cl ions to form AgCl precipitates rather than be reduced to Ag by EG owing to the ultra-low solubility of AgCl. In order to solve this problem, we blend $AgNO_3$ and K_2PtCl_4 in DMF solution at first, and then add ammonia solution to dissolve the generated AgCl and form soluble silver ammonia ions ($[Ag(NH_3)_2]^+$), while $PtCl_4^{2-}$ with some Cl ions removed will transfer into dichlorodiamineplatinum ($Pt(NH_3)_2Cl_2$) with ammonia. And the color of the solution will turn into yellow-green that is the same as that of dichlorodiamineplatinum [39]. Then the Ag ions, Cl ions and Pt salt can be dissolved in DMF simultaneously, no more AgCl precipitation will be produced.

The XRD diffraction patterns of the Ag-Pt/C samples prepared with a precursor solution are displayed in the Figure 2b. The diffraction peaks of AgCl in the Figure 2a are disappeared, indicating that the preparation of the precursor solution can avoid the formation of AgCl precipitation. The locations of diffraction peaks of those three Ag-Pt/C catalysts are all between the pure Pt and pure Ag, which is due to the formation of the Ag-Pt alloys. Since the Ag atoms are doped into pure Pt lattice, the lattice parameter will be changed to one between the lattice parameters of pure Pt and pure Ag, resulting in the change of the positions of XRD diffraction peaks. Moreover, it can be observed that the position of diffraction peaks of the samples is closer to the pure Ag with the increased Ag at.% in the Ag-Pt alloy. In addition, the broad diffraction peak width of the sample implies that the particle size of Ag-Pt alloy in the samples should be expected to be very small. To sum up, the XRD results demonstrate that, by employing the precursor, we successfully prepared Ag-Pt bimetallic nanoparticles with small diameter.

Figure 3 displays the TEM photos of the Ag-Pt/C-15%$_{Ag}$. The TEM images of other samples are displayed in the Figure S1 (see Suporting Information). As we see from the TEM photos, the metal nanoparticles are evenly distributed on the carbon support without distinct aggregation. The average diameter of the nanoparticles is ~ 4 nm (the particle size distribution of the samples are provided in Figure S1 and S2), which is consistent with the prediction of XRD results. The lattice fringes of the nanoparticles are shown in Figure 3c and the lattice spacing of the metal particles is about 0.228 nm, between the spacing of pure Pt (111) (0.2265 nm) and pure Ag (111) (0.2359 nm), indicating that these nanoparticles should be the alloys of Ag and Pt. There are several obvious diffraction rings in the SAED of the sample, which coincide with the diffraction peaks in the XRD pattern. The TEM characterization shows the micromorphology of the Ag-Pt/C sample, proving that the sample is composed of the Ag-Pt alloy nanoparticles loaded on carbon support.

The elemental distribution in the red box on the dark field photo of the Ag-Pt/C-15%$_{Ag}$ samples is scanned and the result is shown in Figure 3e. It is seen that the positions of the nanoparticles in the dark field photo have more signals detected in the elemental mapping, which proves that the nanoparticles in the Ag-Pt/C is composed of Ag and Pt.

We have applied XPS to analyze the distribution of elements and their valence states on the sample surface. The XPS full spectrum, Pt_{4f} and Ag_{3d} spectra of each sample are shown in the Figure S3, and the results of the XPS peak fitting for Pt_{4f} are summarized in the Table S1 (see Suporting Information). According to the statistics, the proportion of the Pt^{2+} on the surface of the metal particles increases with the rise of the Ag atom ratio in the Ag-Pt alloy, which is due to the increase of the number of Pt atoms alloyed with Ag atoms. Together with the XPS results, the characterization results above have proved the formation of the Ag-Pt alloy.

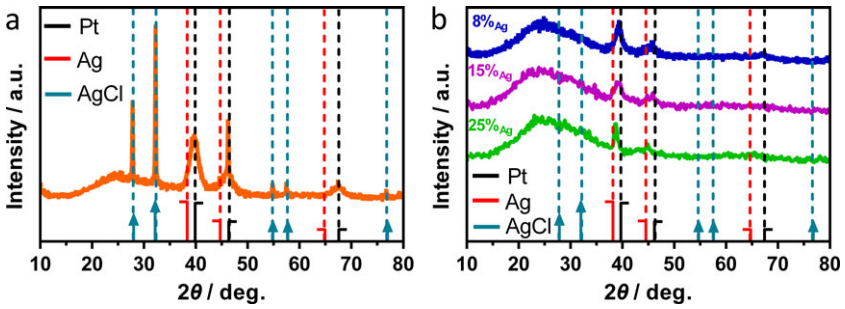

Fig. 2 XRD patterns of the sample made without precursor (a) and the Ag-Pt/C samples with different Ag at.% (b).

In order to compare the performance of the Ag-Pt/C samples with various Ag atomic ratios (Ag-Pt/C-X%$_{Ag}$), the different amount of $AgNO_3$ has been used in the preparation process. The final Ag content of each sample has been tested by the ICP, EDS and XPS methods and summarized in the Table 1. The Ag content in the Ag-Pt alloy increases from 8% to 15%, and about 25%, respectively, with

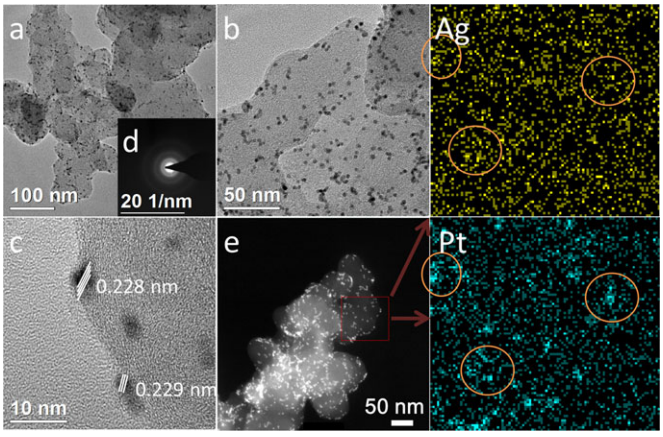

Fig. 3 TEM images (a-c), SAED (d) and element mapping (e) of the Ag-Pt/C-15%$_{Ag}$ sample.

the increase of the $AgNO_3$ usage in the reactants. However, the 25% seems to be the maximum value of the Ag at.%, which may be attributed to the proportion of the Ag-Pt alloy is Pt_3Ag [40].

Next, we compare the atomic ratios obtained by ICP, EDS and XPS to study the distribution uniformity of the elements in the Ag-Pt nanoparticles. The ICP and EDS are analytical methods for analyzing the bulk of the material, so they can measure the overall element content of the samples. Therefore, the results of ICP and EDS are almost the same. However, the atomic ratios measured by XPS are significantly lower than those by other two methods for the samples with Ag of 8 at.% and 15 at.%, while the atomic ratios measured by XPS for the sample with Ag atomic ratio of 25% are similar to those by other methods. The XPS is a method for the surface characterization, so the difference of the results obtained by the three methods indicate that the surface of the Ag-Pt alloy with low Ag atomic ratio is enriched by the Pt atoms, and the Ag atoms are mainly distributed in the inner of the Ag-Pt alloy nanoparticles. On the contrary, the elemental distribution in the Ag-Pt/C-25%$_{Ag}$ is uniform.

3.2 Electrochemical Performance of the Samples

Figure 4 displays the CO stripping curves and the summary of the ECSA for the fresh and aged samples. The commercial Pt/C catalyst (Pt 40 wt.%) is selected as the standard sample for comparison. The CO stripping test indicates that the ECSA of Ag-Pt/C-8%$_{Ag}$ sample is 85.50 $m^2\ g_{Pt}^{-1}$, and it reduces to 61.56 $m^2\ g_{Pt}^{-1}$ after the ADT, losing 28% of its original ECSA. The Ag-Pt/C-15%$_{Ag}$ sample possesses an ECSA of 88.21 $m^2\ g_{Pt}^{-1}$, and after the ADT, the value decreases to 66.16 $m^2\ g_{Pt}^{-1}$, with 75% remaining. The ECSA of the fresh Ag-Pt/C-25%$_{Ag}$ sample is 82.33 $m^2\ g_{Pt}^{-1}$, and 65.04 $m^2\ g_{Pt}^{-1}$ for the aged Ag-Pt/C-25%$_{Ag}$ sample, reduced by 21%. All the Ag-Pt/C samples have higher ECSA than that of the Pt/C (74.49 $m^2\ g_{Pt}^{-1}$) and the Ag-Pt/C-15%$_{Ag}$ sample exhibits the highest value. This is a result of the alloying of Pt and Ag that the doping of Ag reduces the number of inactive Pt atoms inside the nanoparticles, which raise the utilization of Pt and thus the ECSA of the Pt-based catalyst. Besides, the Ag-Pt/C samples also retain more of their ECSA than that of the Pt/C (lose 49% of its ECSA after ADT), which represents the better catalytic stability. It is worth noting, that the retention rate of the ECSA increases with the rise of the Ag atomic ratio of the Ag-Pt/C sample, which manifests that the doping of Ag

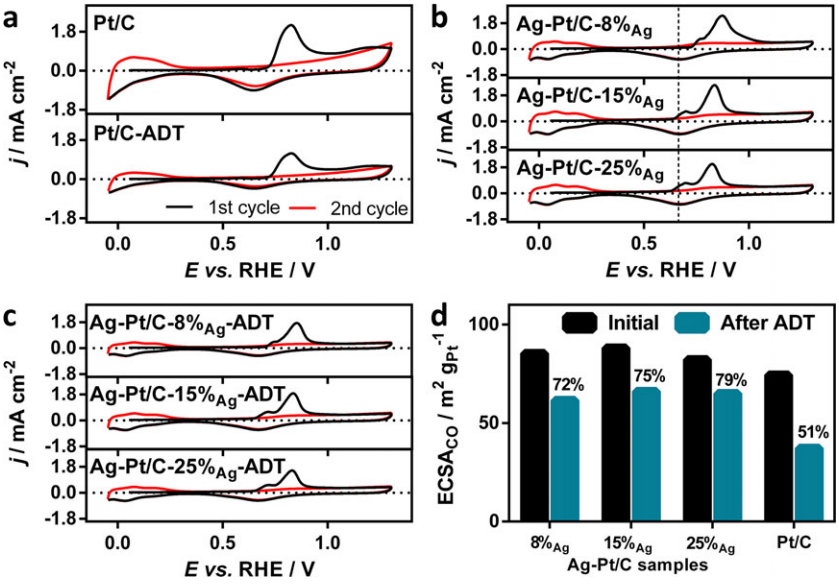

Fig. 4 CO stripping curves of the different samples before and after the ADT (a-c) and the summary of the ECSA (d).

Table 1 The atomic ratios of different samples.

The use of $AgNO_3$ / mg	Ag : Pt in the reactant	Ag : Pt in the product[a]	Ag : Pt in the product[b]	Ag : Pt in the product[c]
1.0	11 : 89	8 : 92	8 : 92	4 : 96
2.0	20 : 80	15 : 85	14 : 86	9 : 91
4.0	33 : 67	24 : 76	25 : 75	-
8.0	50 : 50	27 : 73	26 : 74	25 : 75

[a] ICP analysis results (Table S3).[b] EDS analysis results.[c] XPS analysis results (Figure S3, Table S2).

atoms into the Pt metal will enhance the stability of the Pt metal, and the more the Ag atoms dope, the more stable the Pt metal is.

The LSV curves of the different samples are presented in the Figure 5, which is used to test the catalytic activity of each sample for the ORR. At the beginning of the test, the potential of the electrode sweeps negatively from 1.05 V (*vs.* RHE). Although the oxidation-reduction potential of oxygen is 1.23 V (*vs.* RHE), the overpotential of ORR on the modern catalyst is so large that the ORR can only occur below ~ 0.95 V [23]. The half-wave potential of the Ag-Pt/C-8%$_{Ag}$, Ag-Pt/C-15%$_{Ag}$ and the Ag-Pt/C-25%$_{Ag}$ sample is 21 mV, 43 mV and 79 mV, respectively, more positive than that of the Pt/C, indicating that the overpotential of the ORR is reduced on the Ag-Pt/C catalyst. Furthermore, the Pt mass activities (at 0.9 V *vs.* RHE) of the fresh and aged samples have been calculated and summarized in the Figure 5b and the Table S4. The LSV curves taken after the ADT of the samples are displayed in the Figure S4.

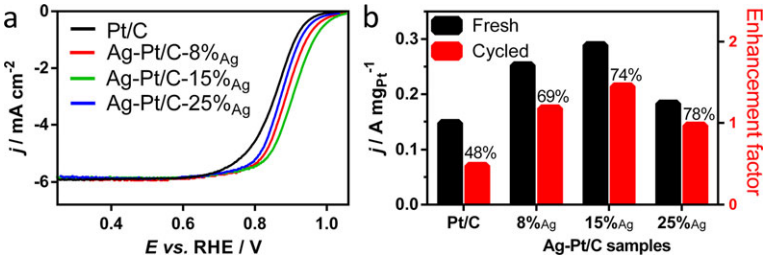

Fig. 5 LSV curves (a) and the summary of the Pt mass activities of the different samples (b).

The Ag-Pt/C-15%$_{Ag}$ sample exhibits the highest Pt mass activity that is about two times higher than that of the Pt/C. With the increase of Ag atomic ratio, the Pt mass activities of Ag-Pt alloy exhibit a tendency to increase at first and then decrease, which shows that the influence of doping Ag atoms on the ORR activity of the samples is complex. The activity retention rate increases with the increase of the Ag atomic ratio, which is the same as the trend observed in the ECSA. This result again proves that the Ag atom in the Ag-Pt alloy can improve the endurance of the Ag-Pt alloy.

It is impressive that the doping of 15 at.% Ag in the Ag-Pt alloy brings an effective enhancement for the ORR activity of Pt alloy catalyst. The oxygen adsorption energy of the (111) plane of the Ag-Pt-25%$_{Ag}$ alloy, the Pt-rich Ag-Pt-15%$_{Ag}$ alloy, and pure Pt metal was obtained by density functional theory (DFT) calculation. The surface of the Ag-Pt-15%$_{Ag}$ alloy has an oxygen adsorption energy of –1.71 eV, while –1.73 eV for the surface of the Ag-Pt-25%$_{Ag}$ alloy, and –1.74 eV for the pure Pt. According to the report of Nørskov et al. [41], the surface of the Pt-based catalyst with a lower oxygen adsorption than that of the pure Pt will exhibit better ORR activity due to the better balance between the adsorption of oxygen and the desorption of oxygenated intermediates during ORR catalysis [42]. The theoretical calculation results together with the experimental results demonstrate that the intrinsic ORR activity of the Ag-Pt alloy surface is better, compared with the pure Pt surface.

It is rather unexpected that, as the Ag content in the Ag-Pt alloy increases, the catalytic activity rises first and then decreases. One reason for the enhancement to the ORR activity by doping Ag atoms into the Pt metal is that the Ag atoms replace a part of the Pt atoms inside the nanoparticles that cannot participate in the ORR catalysis, thereby improving the utilization of Pt. Another reason is the effect of Ag atoms on the electronic structure of Pt atoms, which is verified by the DFT calculation. However, as the content of Ag atoms is further increased, it is found that the ORR activity decreases, which manifests that the high Ag atomic ratio is adverse to the ORR activity of the Ag-Pt alloy. After investigating the literature, we have found the cause that may engender this abnormal phenomenon. For example, Yang et al. have found that the Ag atoms on the Ag-Pt alloy surface have no adsorption activity for oxygen [43]. It can be inferred that the increase of the Ag at.% in the Ag-Pt alloy will raise the number of Ag atoms on the surface of the alloy that cannot adsorb oxygen molecules, and hence the number of catalytic active sites that can simultaneously adsorb oxygen molecule will decline, as shown in Figure 6.

When the Ag at.% is low, the Ag atoms tend to distribute inside the Ag-Pt alloy nanoparticles, so there are only a few Ag atoms on the surface, which will not hinder the oxygen adsorption on the surface. In this occasion, the doping of Ag improves the utilization of Pt without side effect. However, when the Ag at.% of the Ag-Pt alloy increases steadily to 25%, the distribution of Ag atoms becomes uniform, so that there will be one Ag atom in every four atoms on the Ag-Pt alloy surface. At this point, the number of Pt atoms incapable of smoothly adsorbing oxygen will increase, such as the yellow-circled Pt atoms and the yellow-crossed oxygen molecules in Figure 6. That is to say, the overdoping of Ag will hinder the oxygen adsorption on the surface of the alloy. Therefore, although the high Ag doping amount can also increase the utilization of Pt, the hindrance on the adsorption of oxygen is greater, which at last decreases the catalytic activity for the ORR of the Ag-Pt alloy with high Ag at.%.

The ADT results demonstrate that the Ag-Pt alloy catalyst is significantly ascendant to the Pt/C in terms of the catalytic stability. For the Ag-Pt/C samples, after the ADT, not only a high electrochemical surface area remains, but also a high level of performance retention exists. We used TEM to observe the change of the aged Ag-Pt/C-15%$_{Ag}$ sample, as shown in the Figure 7. After 15,000 cycles of potential scanning, some agglomerations appear on the carbon support and the lattice spacing of the agglomeration is 0.227 nm, very close to the

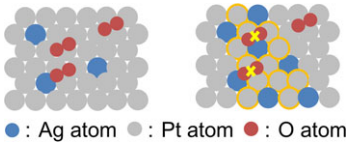

Fig. 6 The Ag-Pt alloy surface with different Ag at.%.

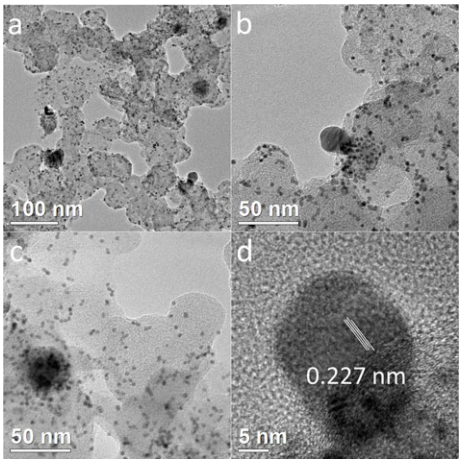

Fig. 7 The TEM images of the cycled Ag-Pt/C-15%$_{Ag}$ sample.

pure Pt, which indicates that some Pt atoms of the Ag-Pt alloy nanoparticles would dissolve and recrystallize during the process of catalyzing the ORR. However, no other obvious change is observed in the remnant nanoparticles, and the Ag-Pt/C sample has basically maintained its original appearance (the size distribution of the cycled sample is shown in Figure S2), thereby remains a high performance. Ramirez-Caballero et al. have used DFT calculations to find that, when the Ag-Pt alloy is formed, the metal bonds between Pt atoms adjacent to Ag and other Pt atoms will become stronger, improving the catalytic stability of Ag-Pt alloy to a certain extent [44]. Our experimental results validate their calculations and demonstrate that the doping of the Ag atoms enhances the stability of Ag-Pt alloy catalyst.

The H_2–O_2 fuel cell polarization curves of the MEA made by the Ag-Pt/C-15%$_{Ag}$ (MEA of Ag-Pt/C) and the commercial Pt/C catalyst (MEA of Pt/C) are shown in the Figure 8. Although the Pt loading of the MEA of Ag-Pt/C is lower than that of the MEA of Pt/C, the voltage drop (140.1 mV) of the MEA of Ag-Pt/C in the activation polarization region (0.000 ~ 0.025 A cm^{-2}) is less than the MEA of Pt/C (186.3 mV). As the composite of the anode side of these two MEA is the same, the difference should come from the better catalytic activity for the ORR of the Ag-Pt/C catalyst used in the cathode side, which lowers the overpotential of the ORR and thus the voltage drop for activating the ORR. Moreover, the maximum power density of the MEA of Ag-Pt/C reaches 186.0 mW cm^{-2}, up to 1.25 times to that of the MEA of Pt/C (148.3 mW cm^{-2}). Considering the Pt loading of the MEA of Ag-Pt/C is lower, the peak Pt mass specific power of the MEA of Ag-Pt/C is 1.33 times to that of the MEA of Pt/C, which is impressive. This result demonstrates that the Ag-Pt/C alloy catalyst can effectively improve the overall power density of the fuel cells owing to its enhanced ORR catalytic activity.

4 Conclusions

In this paper, a simple one-pot approach for the carbon supported Ag-Pt catalyst for the ORR has been reported for the first time. The formation of Ag-Pt alloy is confirmed by means of XRD, EDS, XPS and so on. And different analytical methods are used to find that, in the Ag-Pt alloy with low Ag content, the content of the elements in both the bulk phase and the surface is quite different, indicating that the Ag atom tend to be distributed inside the Ag-Pt alloy nanoparticles. The electrochemical characterization shows that the Ag-Pt/C-15%$_{Ag}$ sample exhibits the highest ORR activity and a better catalytic stability. Furthermore, the MEA used the Ag-Pt/C as the cathode catalyst shows better fuel cell performance than the MEA made from the commercial catalyst, demonstrating the better ORR performance of the Ag-Pt/C. The improvement of the catalytic performance of Ag-Pt alloy is attributed to the doping of the Ag atoms, which increases the utilization of the Pt metal. Furthermore, the theoretical calculation results show that the oxygen adsorption energy on the Ag-Pt alloy surface is slightly lower than that of the pure Pt surface, thus accelerating the desorption of oxygenated intermediates during the catalysis of the ORR, therefore, the catalytic activity for the ORR of the Ag-Pt alloy can be further enhanced. This synthetic method can be instructive for preparing the composite material that combines Ag-Pt alloy catalyst and different kind of carbon support.

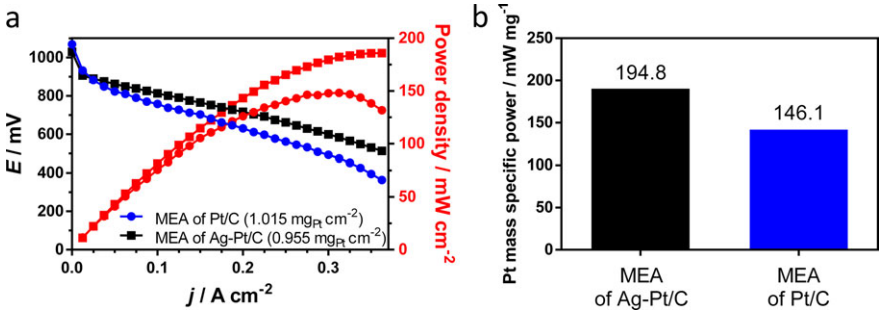

Fig. 8 Polarization curves of the different MEA and the comparison of the Pt mass specific power.

Acknowledgements

Tao Fu and Size Zhang contributed equally to this work and share the first authorship. And we gratefully acknowledge the financial support of the National Natural Science Foundation of China (21621091) and the National Key Research and Development Program of China (2017YFB0102000). And thanks to Prof. Daiwei Liao for his valuable suggestion.

References

[1] Y. Bing, H. Liu, L. Zhang, D. Ghosh, J. Zhang, *Chem. Soc. Rev.* **2010**, *39*, 2184.
[2] J. A. Serfass, *J. Power Sources* **1990**, *29*, 119.
[3] J. Luo, A. H. Jensen, N. R. Brooks, J. Sniekers, M. Knipper, D. Aili, Q. Li, B. Vanroy, M. Wubbenhorst, F. Yan, L. V. Meervelt, Z. Shao, J. Fang, Z. H. Luo, D. E. D. Vos, K. Binnemans, J. Fransaer, *Energy Environ Sci.* **2015**, *8*, 1276.
[4] J. Luo, O. Conrad, I. F. J. Vankelecom, *J. Mater. Chem. A* **2013**, *1*, 2238.
[5] N. M. Markovi, T. J. Schmidt, V. Stamenkovi, P. N. Ross, *Fuel Cells* **2001**, *1*, 105.
[6] Y. Liang, Y. Li, H. Wang, J. Zhou, J. Wang, T. Regier, H. Dai, *Nat. Mater.* **2011**, *10*, 780.
[7] C. Wang, N. M. Markovic, V. R. Stamenkovic, *ACS Catal.* **2012**, *2*, 891.
[8] H. Tang, Y. Zeng, D. Liu, D. Qu, J. Luo, K. Binnemans, D. E. De Vos, J. Fransaer, D. Qu, S. G. Sun, *Nano Energy* **2016**, *26*, 131.
[9] N. Tian, Z. Y. Zhou, S. G. Sun, Y. Ding, Z. L. Wang, *Science* **2007**, *316*, 732.
[10] L. Gan, M. Heggen, R. O'Malley, B. Theobald, P. Strasser, *Nano Lett.* **2013**, *13*, 1131.
[11] V. R. Stamenkovic, B. S. Mun, M. Arenz, K. J. Mayrhofer, C. A. Lucas, G. Wang, P. N. Ross, N. M. Markovic, *Nat. Mater.* **2007**, *6*, 241.
[12] Z. Xu, H. Zhang, S. Liu, B. Zhang, H. Zhong, D. S. Su, *Int. J. Hydrogen Energy* **2012**, *37*, 17978.
[13] T. Schalow, B. Brandt, D. E. Starr, M. Laurin, S. K. Shaikhutdinov, S. Schauermann, J. Libuda, H. J. Freund, *Angew. Chem.* **2006**, *45*, 3693.
[14] S. L. Knupp, M. B. Vukmirovic, P. Haldar, J. A. Herron, M. Mavrikakis, R. R. Adzic, *Electrocatalysis* **2010**, *1*, 213.
[15] M. Shao, T. Yu, J. H. Odell, Mingshang Jin, Y. Xia, *Chem. Commun.* **2011**, *47*, 6566.
[16] M. H. Shao, K. Sasaki, R. R. Adzic, *J. Am. Chem. Soc.* **2006**, *128*, 3526.
[17] K. Gong, F. Du, Z. Xia, M. Durstock, L. Dai, *Science* **2009**, *323*, 760.
[18] L. Qu, Y. Liu, J. B. Baek, L. Dai, *ACS Nano* **2010**, *4*, 1321.
[19] S. Zhang, T. Fu, J. Li, Y. Peng, J. Zhao, *ACS Appl. Energy Mater.* **2018**, *1*, 6198.
[20] L. Ye, K. Wen, Z. Zhang, F. Yang, Y. Liang, W. Lv, Y. Lin, J. Gu, J. H. Dickerson, W. He, *Adv. Energy Mater.* **2016**, *6*, 1502018.
[21] D. Das, R. N. Basu, *J. Am. Ceram. Soc.* **2014**, *97*, 3452.
[22] Y. Shi, A. H. Bork, S. Schweiger, J. L. M. Rupp, *Nat. Mater.* **2015**, *14*, 721.
[23] K. Wen, W. Lv, W. He, *J. Mater. Chem. A* **2015**, *3*, 20031.
[24] V. R. Stamenkovic, B. Fowler, B. S. Mun, G. Wang, P. N. Ross, C. A. Lucas, N. M. Marković, *Science* **2007**, *315*, 493.
[25] Y. J. Wang, N. Zhao, B. Fang, H. Li, X. T. Bi, H. Wang, *Chem. Rev.* **2015**, *115*, 3433.
[26] H. S. Wroblowa, Yen-Chi-Pan, G. Razumney, *J. Electroanal. Chem. Interfacial Electrochem.* **1976**, *69*, 195.
[27] J. A. Keith, G. Jerkiewicz, T. Jacob, *ChemPhysChem* **2010**, *11*, 2779.
[28] J. K. Nørskov, J. Rossmeisl, A. Logadottir, L. Lindqvist, *J. Phys. Chem. B* **2004**, *108*, 17886.
[29] S. M. Foiles, M. I. Baskes, M. S. Daw, *Phys. Rev. B* **1986**, *33*, 7983.
[30] T. Fu, J. Fang, C. Wang, J. Zhao, *J. Mater. Chem. A* **2016**, *4*, 8803.
[31] T. Fu, J. Huang, S. Lai, S. Zhang, J. Fang, J. Zhao, *J. Power Sources* **2017**, *365*, 17.
[32] X. Weng, Q. Liu, J. J. Feng, J. Yuan, A. J. Wang, *J. Colloid Interface Sci.* **2017**, *504*, 680.
[33] A. J. Wang, L. Liu, X. X. Lin, J. Yuan, J. J. Feng, *Electrochim. Acta* **2017**, *245*, 883.
[34] F. Q. Shao, X. Y. Zhu, A. J. Wang, K. M. Fang, J. Yuan, J. J. Feng, *J. Colloid Interface Sci.* **2017**, *505*, 307.
[35] J. Wu, H. Yang, *Acc. Chem. Res.* **2013**, *46*, 1848.
[36] G. Kresse, J. Furthmuller, *Phys. Rev. B* **1996**, *54*, 11169.
[37] P. E. Blöchl, *Phys. Rev. B* **1994**, *50*, 17953.
[38] J. P. Perdew, K. Burke, M. Ernzerhof, *Phys. Rev. Lett.* **1996**, *77*, 3865.
[39] V. Y. Kukushikin, Å. Oskarsson, L. I. Elding, N. Farrell, S. Dunham, S. J. Lippard, *Inorg. Synth.* **1998**, *32*, 141.
[40] Y. Ma, P. B. Balbuena, *Surf. Sci.* **2008**, *602*, 107.
[41] J. Greeley, I. E. L. Stephens, A. S. Bondarenko, T. P. Johansson, H. A. Hansen, T. F. Jaramillo, J. Rossmeisl, I. Chorkendorff, J. K. Nørskov, *Nat. Chem.* **2009**, *1*, 552.
[42] M. Luo, S. Guo, *Nat. Rev. Mater.* **2017**, *2*, 17059.
[43] H. You, Z. Peng, J. Wu, H. Yang, *Chem. Commun. (Camb)* **2011**, *47*, 12595.
[44] G. E. Ramirez-Caballero, Y. Ma, R. Callejas-Tovar, P. B. Balbuena, *Phys. Chem. Chem. Phys.: PCCP* **2010**, *12*, 2209.

